Available online at www.sciencedirect.com
SCIENCE DIRECT®
Journal of Magnetic Resonance 163 (2003) 277–287
JMR Journal of Magnetic Resonance
www.elsevier.com/locate/jmr

Retrospective intra-scan motion correction

Marc E. Bourgeois,[a] Frank T.A.W. Wajer,[b] Muriel Roth,[c] André Briguet,[a] Michel Décorps,[c] Dirk van Ormondt,[b] Christoph Segebarth,[c] and Danielle Graveron-Demilly[a,*]

[a] *Laboratoire de RMN, CNRS UMR 5012, Université Claude Bernard LYON I, CPE, Domaine scientifique de la Doua, 3 rue Victor Grignard, F-69616 Villeurbanne, France*
[b] *Applied Physics Department, Delft University of Technology, Delft, The Netherlands*
[c] *Unité Mixte INSERM/UJF U594, LRC CEA, CHU A. Michallon, Grenoble, France*

Received 8 January 2003; revised 24 April 2003

Abstract

This paper analyzes the effects of intra-scan motion and demonstrates the possibility of correcting them directly in *k*-space with a new automatic retrospective method. The method is presented for series of 2D acquisitions with Cartesian sampling. Using a reference *k*-space acquisition (corrected for translations) within the series, intra-scan motion parameters are accurately estimated for each trajectory in *k*-space of each data set in the series resulting in pseudo-random sample positions. The images are reconstructed with a Bayesian estimator that can handle sparse arbitrary sampling in *k*-space and reduces intra-scan rotation artefacts to the noise level. The method has been assessed by means of a Monte Carlo study on axial brain images for different signal-to-noise ratios. The accuracy of motion estimates is better than 0.1° for rotation, and 0.1 and 0.05 pixel, respectively, for translation along the read and phase directions for signal-to-noise ratios higher than 6 of the signals on each trajectory. An example of reconstruction from experimental data corrupted by head motion is also given.

Keywords: Motion artefacts; Intra-scan motion correction; Post-processing; Image reconstruction

1. Introduction

Subject motion is a major issue in many MRI studies. Several methods have been proposed to reduce the motion artefacts in the individual images or in time series of images [1–13]. Broadly speaking, those methods either aim at reducing the motion at acquisition (use of gating or triggering and/or use of ultra-fast imaging techniques) or following acquisition (post-processing). The post-processing methods aim at estimating the motion-free images from the motion-corrupted data sets. Data corruption occurring between successive acquisitions of imaging volumes in a time series is dealt with with inter-scan motion correction procedures. The latter assume for simplicity that no (intra-scan) motion occurs during acquisition of the data pertaining to the individual volumes. This hypothesis may in certain cases be optimistic and considerable improvements in image quality may be expected if intra-scan motion is also corrected for. In the present paper, we therefore address the problem of intra-scan motion correction, under the simplifying assumption that no motion occurs during the measurement of the data along the successive trajectories in *k*-space. To simplify matters, we have dealt with in-plane, intra-scan motion. We determine the in-plane translations and rotations that occurred between measurements of the data along the successive trajectories in *k*-space, correct for these motions and eventually estimate the motion-free image.

Several methods have been proposed to tackle the different challenges involved in intra-scan motion detection and correction. The correction of in-plane intra-scan translations has been reported in [1–4,14]. Navigator echoes in association with markers [5] or with

* Corresponding author. Fax: +33(0)4-72-44-81-99.
E-mail address: danielle.graveron@univ-lyon1.fr (D. Graveron-Demilly).

1090-7807/$ - see front matter © 2003 Elsevier Science (USA). All rights reserved.
doi:10.1016/S1090-7807(03)00154-X

a circular sampling scheme [6,7] have been proposed for determining rotational and translational motion. Recently, spherical navigator echoes have been introduced [8] in order to address the inability of the orbital navigator echo to measure motion out of its plane. Intra-scan rotation leads to pseudo-randomly sampled k-space [15,16]. Several reconstruction techniques to compensate for artefacts caused by small angle rotations [9,10], or with no limitations on the extent of the rotation angles using either the projection onto convex sets (POCS) [11,13] or a comparison with a reference k-space [12,15–17], have been reported.

In the present study, we show that estimating and correcting retrospectively intra-scan motion is feasible from the information available in k-space [12,15,16]. Two main issues are addressed: (1) the automatic estimation of motion parameters from k-space data along individual trajectories and (2) the accurate reconstruction of images from pseudo-randomly sampled k-spaces. First, the intra-scan translation and rotation parameters for each data-set in a series are estimated by comparing the potentially corrupted data-set with a reference acquisition chosen *within* the series; note that the latter is first corrected for translations. Due to the rotation effects, the resulting 'true' sampling grid is pseudo-random. Finally, after translation correction, the 'motion-free' image is reconstructed using the 'true' sampling grid. The image reconstruction uses Bayesian estimation, originally developed to deal with under-sampled and irregular MRI acquisitions [12,16,18,19]. The present analysis has focused on 2D acquisition with Cartesian sampling (spin-warp imaging). The extension of the method to 3D acquisition with EPI-like techniques is briefly discussed.

In the first part of the paper, the effect of in-plane intra-scan motion is discussed, and the algorithm proposed for motion correction is described in detail. In the second part of the paper, the performance of the motion estimators on axial brain images in the presence of noise is assessed using a Monte Carlo approach and the estimators are 'tuned'.

2. Method

2.1. Two-dimensional intra-scan motion effects in k-space

Consider a 2D Cartesian sampling grid G_C in k-space made up of N rectilinear trajectories (Fig. 1a) and $S_{\text{ref}}(\mathbf{k})$, the reference MRI signal from a solid and static object. Each in-plane gross movement can be described in terms of a rotation R_α of angle α about the centre of the field of view (FOV) and a translation vector $\mathbf{T}$. Assuming that the motion occurs between measurements of the successive rectilinear trajectories, the corrupted signal $S_{\alpha_j,\mathbf{T}_j}(\mathbf{k}_j)$ along the jth trajectory is a function of the reference signal S_{ref}

$$S_{\alpha_j,\mathbf{T}_j}(\mathbf{k}_j) = S_{\text{ref}}(\mathbf{R}_{\alpha_j}^{-1}\mathbf{k}_j)\exp[-2i\pi(\mathbf{R}_{\alpha_j}^{-1}\mathbf{k}_j).\mathbf{T}_j], \quad (1)$$

where $\mathbf{T}_j$ and $\mathbf{R}_{\alpha_j}$, respectively, the translation vector and the rotation operator for the rotation of angle α_j about the centre of the FOV, describe the position of the object during the acquisition of the jth echo. Our algorithm is directly based on the analysis of this equation. It can be deduced from Eq. (1) that: (1) a translation of the object induces a phase term which is linear along the readout direction and depends on the rotation; and (2) a rotation $\mathbf{R}_{\alpha_j}$ of the object in image space is equivalent to a rotation $\mathbf{R}_{\alpha_j}$ of the signal about the centre of k-space. While the signal magnitude is only affected by the rotation, the phase of the signal is modified by both rotation and translation. Thus the phase difference between $S_{\alpha_j,\mathbf{T}_j}(\mathbf{k}_j)$ and $S_{\text{ref}}(\mathbf{R}_{\alpha_j}^{-1}\mathbf{k}_j)$ induced by the translation $\mathbf{T}_j$ is linear

$$\Phi_{\alpha_j,\mathbf{T}_j}(\mathbf{k}_j) = -2\pi[\mathbf{R}_{\alpha_j}^{-1}\mathbf{k}_j].\mathbf{T}_j. \quad (2)$$

The components T_{jx} and T_{jy} of the translation vector are, respectively, the component along the jth trajectory direction (readout direction) and the component perpendicular to the readout direction (phase encoding direction). As different intra-scan rotations may occur during the scan time, the signals are acquired in k-space on non-parallel directions leading to *pseudo-random* sampling [12,16] (Fig. 1b). In the following, this pseudo-random acquisition grid will be noted G_α. Consequently, if directly applied, the 2D-FFT reconstruction leads to artefacts in the images.

2.2. Motion correction algorithm

To correct for in-plane intra-scan gross motion, the method has to compensate the linear phase variations along the acquisition trajectories of G_α and to reconstruct the image considering that the signal has been sampled on an pseudo-random grid G_α. The algorithm compares the motion-distorted signal $S_{\alpha_j,\mathbf{T}_j}(\mathbf{k}_j)$ to the reference signal $S_{\text{ref}}(\mathbf{k}_j)$ so that the motion parameters for each trajectory j can be estimated. This information is then used to reconstruct the motion-free image. We therefore assume that a reference signal $S_{\text{ref}}(\mathbf{k}_j)$ has been acquired or estimated. The algorithm thus involves five steps:

(1) Construction of the reference signal.
(2) Estimation of the rotation angle set $\{\alpha_j\}$, $j \in \{-N/2+1, N/2\}$. The estimated angles $\hat{\alpha}_j$ define an estimated acquisition grid $\hat{G}_\alpha$.
(3) Estimation of the $2N$ translation parameters T_{jx}, T_{jy} using the estimated acquisition grid $\hat{G}_\alpha$. This leads to the estimates $\hat{T}_{jx}$ and $\hat{T}_{jy}$.
(4) Compensation of the linear phase shifts induced by the translations on the estimated grid $\hat{G}_\alpha$.
(5) Reconstruction of the image with a Bayesian estimator using the translation-corrected signal sampled on the estimated sampling grid $\hat{G}_\alpha$.

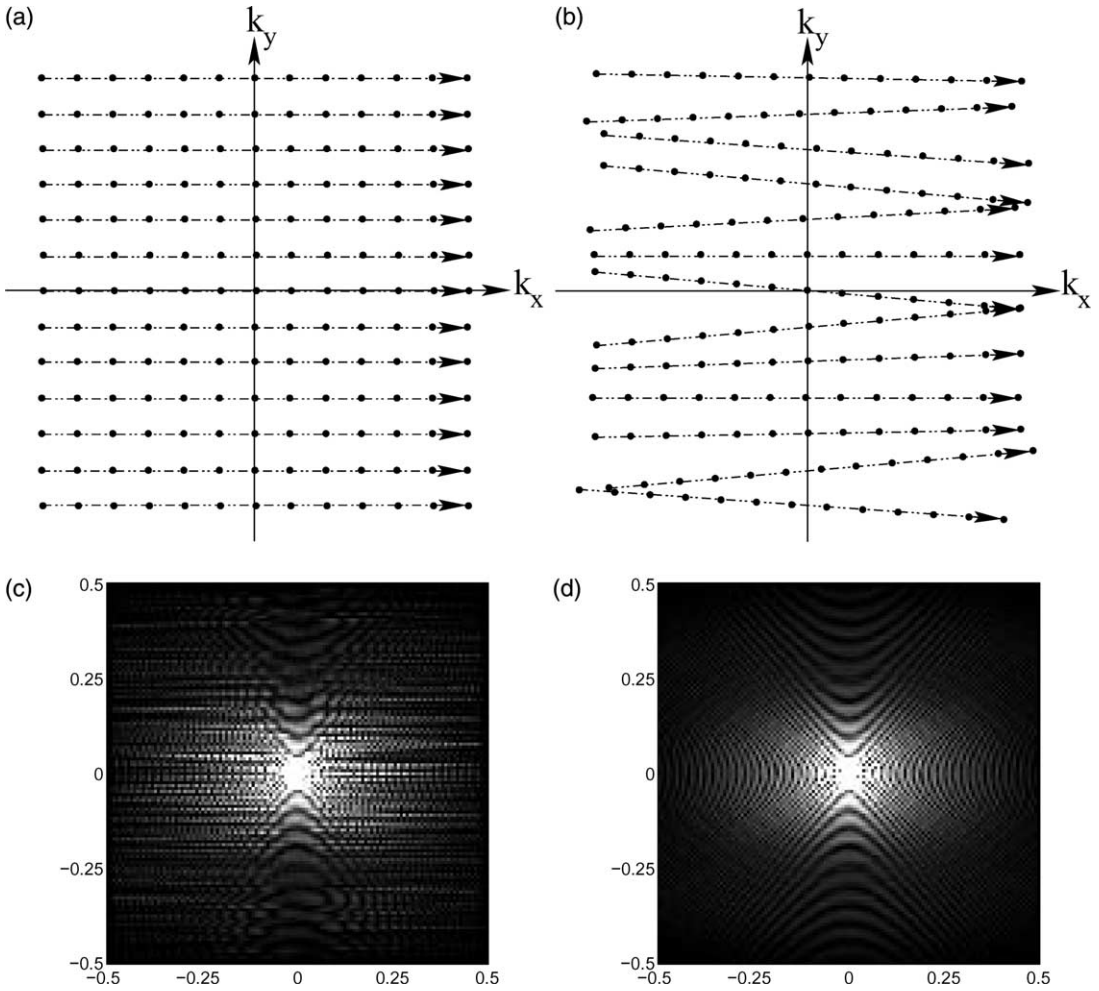

Fig. 1. (a) Cartesian sampling grid G_C and (b) rotation-corrupted grid G_α. (c) Shepp–Logan phantom in the k-space with intra-scan rotations simulated by rotating each trajectory of k-space with random angles characterized by a Gaussian distribution ($\mu = 0$, $\sigma = 1.0°$). (d) k-Space after Bayesian reconstruction of the rotation-corrupted k-space in (c).

These steps are described in detail in the following sections.

2.2.1. Construction of the reference signal

A priori, motion is expected to distort all images in a series. A difficulty in correcting intra-scan motion, therefore, is the lack of an ideal reference signal, i.e., a signal acquired without any motion distortion. Since the estimation of the motion parameters relies on a comparison of the reference signal with the distorted one, the accuracy of the estimates will depend on the quality of the reference signal. The first step of the algorithm therefore aims at optimizing the quality of one particular acquisition in the series (for instance the first one) by correcting the artefacts due to the translations (this operation does not require any reference signal) and use the corrected data as reference data for the series. To correct the translation-induced linear phase differences of the signals along k-space trajectories, we have used our own implementation of the algorithm of Gerchberg and Saxton [1,3,20]. Details concerning our translation estimation algorithm will be presented in the following section.

2.2.2. Estimation of the rotation angles

To estimate the rotation angles $\{\alpha_j\}$, the magnitudes of the distorted signal $|S_{\alpha_j,\mathbf{T}_j}(\mathbf{k}_j)|$ and of the reference signal $|S_{\text{ref}}(\mathbf{k}_j)|$ are compared for each trajectory j. Note that translation does not affect the magnitude of the distorted signal (see Eq. (1)). The comparison is done by maximizing the correlation coefficient $C_j(\theta)$ between $|S_{\alpha_j,\mathbf{T}_j}(\mathbf{k}_j)|$ and the reference signal, regridded on the rotated grid G_θ: $|S_{\text{ref}}(\mathbf{R}_\theta^{-1}\mathbf{k}_j)|$ ($\mathbf{R}_\theta$ is the rotation operator of angle θ). A gridding algorithm [12,19,21,22] was used to resample the reference signal onto the rotation-corrected grids. Because resampling is done from a Cartesian (rectangular) grid onto an irregular grid, the error induced by the gridding algorithm is negligible [19,23,24], see gridding section below. For each trajectory j, the maximum of $C_j(\theta)$ is first estimated by

calculating it for M different rotation angles θ. The maximization is then refined by fitting $C_j(\theta)$ with a polynomial of degree 2. In practice, 80 values ($M = 80$) of θ were chosen in the range $[-5^\circ, +5^\circ]$ corresponding to the expected motion range occurring in, e.g., fMRI.

This first step leads to the estimated angle set $\{\widehat{\alpha_j}\}$ and defines the estimated acquisition grid $\hat{G}_\alpha$. Information regarding the rotations is also required to estimate the translation parameters since the rotations indirectly modify the phase of the signal (see Eq. (2)).

2.2.3. Estimation of the translations and compensation of the linear phase shifts

Equation (2) indicates that in order to correct the translation effects, the algorithm has to compensate the linear phase $\Phi_{\alpha_j,\mathbf{T}_j}(\mathbf{k}_j)$ induced by the translation along each trajectory of the acquisition grid G_α. This phase must be separated from the object signal-phase. Therefore, the phase of the reference signal $S_{\text{ref}}(\mathbf{k}_j)$ is compared with the one of the distorted signal $S_{\alpha_j,\mathbf{T}_j}(\mathbf{k}_j)$. This operation requires that both signals be sampled on the same grid G_α. Thus $S_{\text{ref}}(\mathbf{k}_j)$ must first be resampled on the grid $\hat{G}_\alpha$. This operation is also done using the gridding algorithm. Finally, the phase due to translation motion is obtained by computing

$$\Phi_{\alpha_j,\mathbf{T}_j}(\mathbf{k}_j) = -\arg\left\{S_{\text{ref}}(\mathbf{R}^{-1}_{\hat{\alpha}_j}\mathbf{k}_j)(S_{\alpha_j,\mathbf{T}_j}(\mathbf{k}_j))^*\right\}. \tag{3}$$

One way to estimate the translation $\mathbf{T}_j$ would be to linearly fit the phase $\Phi_{\alpha_j,\mathbf{T}_j}(\mathbf{k}_j)$ as a function of k_j. In order to avoid unwrapping process which may be difficult for low signal-to-noise ratios, we preferred to fit $\sin(\Phi_{\alpha_j,\mathbf{T}_j}(\mathbf{k}_j))$ as a function of k_j using a nonlinear least squares minimisation (Marquardt algorithm). In this way, the phase $\Phi_{\alpha_j,\mathbf{T}_j}(\mathbf{k}_j)$ is estimated for each trajectory j, providing $\hat{\Phi}_{\hat{\alpha}_j,\hat{\mathbf{T}}_j}(\mathbf{k}_j)$. The linear phase of the signal $S_{\alpha_j,\mathbf{T}_j}(\mathbf{k}_j)$ is finally compensated by means of the phase factor $\hat{\Phi}_{\hat{\alpha}_j,\hat{\mathbf{T}}_j}(\mathbf{k}_j)$ leading to $\hat{S}_{\alpha_j}(\mathbf{k}_j)$:

$$\hat{S}_{\alpha_j}(\mathbf{k}_j) = S_{\alpha_j,\mathbf{T}_j}(\mathbf{k}_j)\exp(i\hat{\Phi}_{\hat{\alpha}_j,\hat{\mathbf{T}}_j}(\mathbf{k}_j)). \tag{4}$$

After this step, the signal $\hat{S}_{\alpha_j}(\mathbf{k}_j)$ remains affected only by the rotation. Thus, the image can be reconstructed by a method capable of processing pseudo-randomly sampled data.

2.2.4. Reconstruction of the image on a Cartesian grid

The correction of rotational motion requires resampling the k-space signal $\hat{S}_{\alpha_j}(\mathbf{k}_j)$, $j = 1, N$ from the estimated grid $\hat{G}_\alpha$ to a Cartesian grid G_{C}.

Gridding. Because extensive use was made of gridding, a few points deserve to be addressed. One can distinguish two cases: (1) Gridding from a Cartesian (rectangular) grid onto an irregular grid, hereafter referred to as *reverse* gridding. (2) Gridding from an irregular grid onto a Cartesian grid, hereafter referred to as conventional gridding. The accuracy of gridding depends on the accuracy of the concomitant sampling density correction. In case 1 there is no need for the sampling density compensation because each Cartesian grid-point represents the same area (in 2D). The sampling density compensation for case 2 can be problematic, especially for randomly positioned grid-points. As a consequence, reverse gridding can be much more accurate than conventional gridding. In fact, it amounts to sinc-interpolation (Shannon theorem), the accuracy of which can be adapted to the task at hand by proper setting of its parameters [23,24]. We mention here that simulation of rotation of k-space grid-points was done with reverse gridding too.

Moreover, because a pseudo-random sampling distribution is not a shah function, its Fourier Transform (FT) is not periodic. Furthermore, the FT of a sparse sampling distribution (i.e., barely satisfying the Nyquist condition) exhibits interpolation artefacts within, as well as outside, the FOV [12,16,19]. Since gridding is unable to attenuate interpolation artefacts within the FOV, it is not well suited to resample pseudo-randomly and sparsely sampled k-space signals. Therefore, we resort to a Bayesian estimation [12,18,23,25,26] which enables reconstruction from arbitrary sample positions in k-space.

Bayesian estimation. The Bayesian reconstruction method has been described in detail in [12,19,27,28]. Briefly, the reconstruction algorithm aims at determining the image I on a Cartesian grid given the signal and available prior knowledge, which maximizes the posterior probability density function $P(I|S)$, where I and S are the reconstructed image and measured k-space signal on the grid G_α, respectively. This leads to the image I which is the most probable image given the signal S. Using the Bayes-theorem, $P(I|S)$ may be written as follows

$$P(I|S) = \frac{P(S|I)P(I)}{P(S)}. \tag{5}$$

We may equally well, maximize $\log P(I|S)$ instead of $P(I|S)$, and so our aim is to calculate

$$\max_I\{\log P(S|I) + \log P(I)\}. \tag{6}$$

In the above, the *evidence* $P(S)$ was treated as a constant because it does not depend on I. The *prior*, $P(I)$, describes any a priori knowledge we have about the image. In this case, a Lorentzian distribution of nearest-neighbour intensity differences was used for the *prior*. $P(S|I)$ is the *likelihood* function and describes the influence of the measurement noise. The algorithm iteratively modifies the image I according to the Lorentzian model while preserving the measured signal S.

The likelihood. The k-space signal and image are related to each other through the 2D Fourier-transform. In addition, the samples in k-space are contaminated by additive, white, Gaussian noise with zero mean and standard deviation σ. We therefore model our data as

$$\boldsymbol{s} = T\boldsymbol{i} + \boldsymbol{n}, \tag{7}$$

in which $T_{m,n} = \exp(-2\pi i(x_n k_{x_m} + y_n k_{y_m}))$ and $\boldsymbol{n}$ is the measurement noise. For ease of notation, we have rewritten the image and data matrices as vectors by stacking their respective columns on top of each other. (x_n, y_n) are the locations of the pixels, which are assumed to be distributed uniformly over a Cartesian grid. Arbitrary, irregular sample positions (k_{x_m}, k_{y_m}) are allowed. Should the (k_{x_m}, k_{y_m}) coincide with a Cartesian grid, T reduces to a 2D FFT. When the (k_{x_m}, k_{y_m}) are pseudo-random, straight-forward calculation of $T\boldsymbol{i}$ is very expensive. A solution to this problem is to use the reverse gridding algorithm. The matrix T is then the product of a regridding matrix with a 2D FFT matrix. Note that T transforms from a Cartesian grid in image space onto an irregular grid in k-space. Hence, estimation of sparse random-sampling density compensation is obviated, yielding increased image quality.

Given the Gaussian nature of the measurement noise we have the following expression for the likelihood-term

$$\log P(S|I) = -\frac{|\boldsymbol{s} - T\boldsymbol{i}|^2}{2\sigma^2}. \tag{8}$$

The prior. Intra-scan rotations cause local under-sampling, then locally violating Nyquist's sampling criterion. The consecutive ill-effect can be alleviated by incorporation of prior knowledge about the image into the reconstruction algorithm. We exploit the knowledge that a histogram of intensity differences of nearest neighbour pixels, ${}^{x}\Delta_{x,y} = I_{x,y} - I_{x-1,y}$ and ${}^{y}\Delta_{x,y} = I_{x,y} - I_{x,y-1}$ has approximately a 2D (3D) Lorentzian shape [12,19,25,29,30]. Note that on purely mathematical grounds in the context of regularization, one arrives at the Lorentzian distribution [31–33]. The corresponding probability distribution for 2D images is

$$P(I) = \prod_{x,y} \frac{a}{2\pi(a^2 + ({}^{x}\Delta_{x,y})^2 + ({}^{y}\Delta_{x,y})^2)^{1.5}}. \tag{9}$$

Substituting Eq. (9) in Eq. (6), while ignoring any constant terms, we get the following optimization problem

$$\min_{I} \left\{ \frac{|\boldsymbol{s} - T\boldsymbol{i}|^2}{2\sigma^2} + \frac{3}{2} \sum_{x,y} \log \left\{ a^2 + ({}^{x}\Delta_{x,y})^2 + ({}^{y}\Delta_{x,y})^2 \right\} \right\}. \tag{10}$$

The image I which results from Eq. (10) is the reconstructed image. The minimization is done with the conjugate gradient method. Details concerning the algorithm, including computational aspects, can be found in [28].

3. Results

In this section, the behaviour of the intra-scan motion estimator is studied as a function of the signal-to-noise ratio (SNR). This study is based on a set of 2D axial brain images presenting simulated intra-scan motion artefacts.

3.1. Image simulations

To simulate the effect of intra-scan rotation on MR data, we used the reverse gridding algorithm. Its accuracy could be set according to need. This has been assessed using an analytically defined Shepp and Logan phantom [34]. T tests and F tests on the distorted signals obtained analytically and by gridding showed not significant difference [23,35]. Thus, we conclude that we may use the reverse gridding algorithm to simulate the rotation artefacts.

As starting image, we have used an axial brain image acquired at 1.5T using a conventional FLASH sequence. The following parameters were used: $TE/TR = 40/77$ ms, flip angle = 30°, slice thickness = 7 mm, number of averages = 32, FOV = $220 \times 220\,\text{mm}^2$, matrix = 64^2. The statistical distributions of the simulated motion parameters used are Gaussian centred with a standard deviation $\sigma_\alpha = 0.5°$ for the rotations and $\sigma_T = 0.25$ pixel for the translations (corresponding to a displacement of 0.8 mm for an 64×64 image with a FOV of 220 mm). Finally, Gaussian noise was added to the complex image to generate images presenting different signal-to-noise ratios SNR_I. This SNR_I was defined as

$$\text{SNR}_I = \frac{1/N_{\text{object}} \sum_{n=0}^{N_{\text{object}}-1} |I[n]|}{\sigma_{\text{noise}}}, \tag{11}$$

where N_{object} is the number of pixels inside the object I. We have similarly, defined the SNR in k-space which will be useful in evaluating the algorithm. For a Cartesian-sampled data set, the SNR is larger for the trajectories near to the centre of k-space (low k_y values) than for those near to the edges (high k_y values). Consequently, the signal on each trajectory was characterized by its own SNR, noted SNR_k and the motion estimator performance was studied as a function of SNR_k. This ratio is defined for the jth trajectory by

$$\text{SNR}_k = \frac{1/N \sum_{n=0}^{N-1} |S[\mathbf{k}_j[n]]|}{\sigma_{\text{noise}}}, \tag{12}$$

where N is the number of samples of a trajectory and σ_{noise}, the standard deviation of the Gaussian noise.

3.2. Optimization of the motion estimators: a Monte Carlo study

3.2.1. Influence of the noise on motion estimators

The precision of the parameter estimates $\hat{\boldsymbol{p}}_j = \{\hat{\boldsymbol{\alpha}}_j, \hat{\mathbf{T}}_j\}, j \in \{-N/2+1, N/2\}$ depends on the signal-to-noise ratio SNR_k of the trajectory signal considered. Below a particular threshold SNR_T of the signal-to-noise ratio, the noise-related errors $\epsilon_{p_j} = p_j - \hat{p}_j$ can be

larger than the standard deviation σ_p of the parameter distribution itself. In this case, motion correction based on $\hat{p}_j$ is likely to degrade rather than improve the image. It is thus preferable to not correct in those cases and to use $\hat{p}_j = 0$. The threshold signal-to-noise level, $\mathrm{SNR_T}$, below which the estimate $\hat{p}_j$ is rejected, was defined as the SNR_k value for which the following probability equation was verified

$$P(|\epsilon_{p_j}(\mathrm{SNR}_k)| \leqslant \sigma_p) = P(|p_j| \leqslant \sigma_p), \tag{13}$$

where P represents a probability function. If the motion parameters are considered to follow normal distributions, the second term of the Eq. (13) is equal to 0.683. For each trajectory j, the following rules were applied:

- if $\mathrm{SNR}_k \geqslant \mathrm{SNR_T}$, the estimate $\hat{p}_j$ was retained,
- if $\mathrm{SNR}_k < \mathrm{SNR_T}$, the estimate $\hat{p}_j$ was replaced by 0.

Applying these rules produces the new set of estimated parameters $\{\tilde{p}_j\}$. The threshold $\mathrm{SNR_T}$ was determined by means of a Monte Carlo study as follows.

A set of 160 motion-corrupted brain k-space signals (64×64) sampled on different grids G_α and having different levels of Gaussian noise (SNR_I in the range $[50, 370]$), was simulated. This led to a global set of 10,240 (160×64) trajectory signals covering a large range of SNR_k. For each k-space, each trajectory signal resulted from a pseudo-random rotation and translation with standard deviations $\sigma_\alpha = 0.5°$ and $\sigma_T = 0.25$ pixel, respectively. The global set of 10,240 k-space signals (10,240 different rotation angles and translations) was then split into subsets corresponding to SNR_k intervals of 0.1. For each SNR_k interval between 0 and 10, we have thus obtained more than 20 signals whose motion parameters have been estimated. The subsets were used to assess the effect of an $\mathrm{SNR_T}$ threshold on the accuracy of the rotation and translation estimations. The next two paragraphs present the results for each estimator.

3.2.2. Optimization of the rotation estimator

To assess the performance of the rotation estimator, the mean value $\mu_{\epsilon_{\hat{\alpha}}}$ and the standard deviation $\sigma_{\epsilon_{\hat{\alpha}}}$ of the error $\epsilon_{\hat{\alpha}} = \alpha_j - \hat{\alpha}_j$ were computed from the 10,240 estimates of the rotation angles, as a function of SNR_k. These statistical values were normalized with respect to the standard deviation σ_α of the rotation angle distribution. The results in Fig. 2a show that the rotation estimator is unbiased and that the accuracy (standard deviation error) of the estimates is better than 0.1° for SNR_k values higher than 6 (80% of the signals with this data set). Moreover, the standard deviation $\sigma_{\epsilon_{\hat{\alpha}}}$ becomes larger than σ_α for $\mathrm{SNR}_k < 1$. The noise threshold $\mathrm{SNR_T}$ can also be deduced from the plot of the probability $P(|\epsilon_\alpha| \leqslant \sigma_\alpha)$ for estimating a rotation angle with an error less than σ_α versus the noise level SNR_k (see Fig. 2b). The threshold $\mathrm{SNR_T}$ for which $P(|\epsilon_\alpha| \leqslant \sigma_\alpha)$ equals 0.683, is approximatively 1. In practice the estimated SNR_k overestimates the true SNR because the magnitude of the signal is used in Eq. (12). This estimation is affected by an error which depends on the noise level. At low SNR, the estimated mean value of the signal magnitude follows a Rician distribution [36]. Thus, if $\mathrm{SNR}_k = 1$, 70% of SNR_k estimates will be in fact larger than 1 and, using the threshold $\mathrm{SNR_T} = 1$, only 30% of estimated angles would be rejected instead of 100% expected. In order to increase this ratio to 90%, we fixed the threshold $\mathrm{SNR_T}$ to 2.7. The use of this SNR threshold leads to a new estimated grid denoted $\tilde{G}_\alpha$.

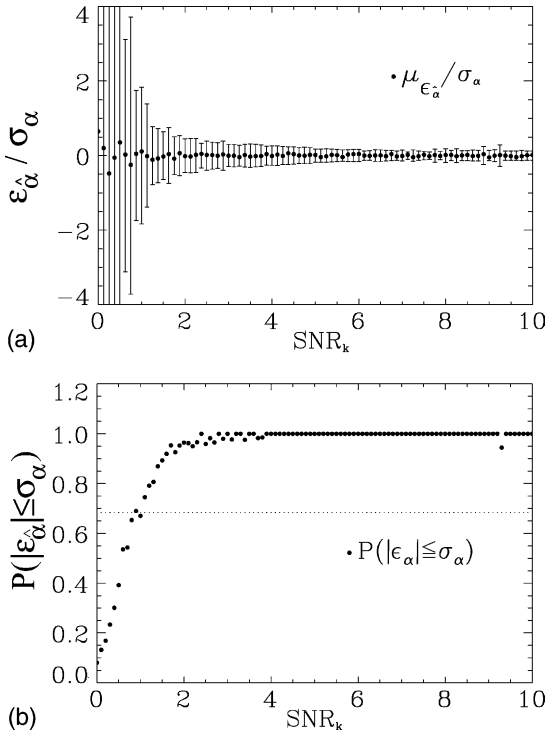

Fig. 2. Behaviour of rotation angle estimator. (a) Statistical estimation error as a function of the noise level SNR_k: mean error $\mu_{\epsilon_{\hat{\alpha}}}/\sigma_\alpha$ (•) and standard deviation error $\sigma_{\epsilon_{\hat{\alpha}}}/\sigma_\alpha$ (error bars). The statistical values were normalized with respect to the rotation angle standard deviation σ_α. (b) Probability of estimating a rotation angle with an error less than the standard deviation σ_α of the rotation angle distribution versus the noise level SNR_k; $\sigma_\alpha = 0.5°$.

3.2.3. Evaluation of the translation estimator

The translation estimator was tested similarly as a function of SNR_k. Our studies showed that its behaviour is not significantly affected by the error of rotation estimation. Therefore, the results presented here characterize the translation estimates obtained from simulations including rotations, and using the estimated grid $\tilde{G}_\alpha$. Again, it appears that the estimator is unbiased (see Fig. 3a and b). For $\mathrm{SNR}_k \geqslant 6$ the error $\epsilon_{\hat{T}_{jx}} = T_{jx} - \hat{T}_{jx}$ on the estimation of T_{jx} is less than 0.1 pixel and the error $\epsilon_{\hat{T}_{jy}} = T_{jy} - \hat{T}_{jy}$ is less than 0.05 pixel. Fig. 3c shows that there is no need to introduce a noise threshold in the translation estimator since the probability to esti-

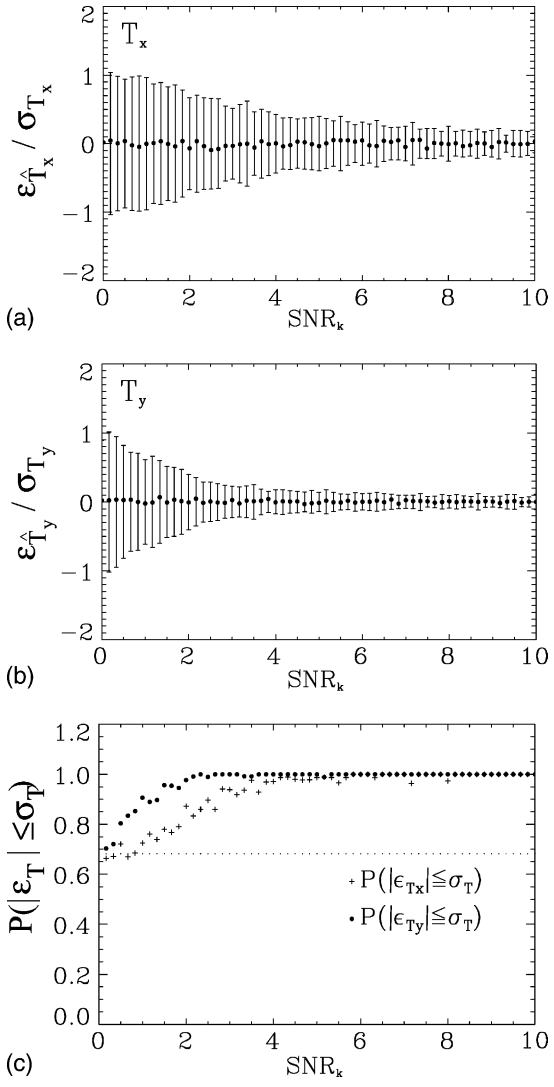

Fig. 3. Behaviour of the translation estimator. Errors on the estimates T_x (a) and T_y (b) as a function of the noise level SNR_k: mean error $\mu_{\epsilon_T/\sigma_T}$ (•), and standard deviations error $\sigma_{\epsilon_T}/\sigma_T$ (error bars). The statistical values were normalized with respect to the translation standard deviation σ_T. The graph (c) shows the probabilities to estimate the translations T_x and T_y with an error smaller than σ_T, versus the noise level SNR_k; $\sigma_T = 0.25$.

mate the translation with an error lower than the standard deviation σ_T is greater than 0.68 even for low SNR_k.

3.3. Performance of the motion correction

In order to evaluate the performance of the motion correction, we have chosen a criterion, based on the root mean square error in the object [29,30]

$$\mathrm{NRMSE}_{\mathrm{object}}(I) = \frac{1}{\sqrt{\sigma_{I_{\mathrm{ref}}}^2 + \sigma_I^2}} \sqrt{\frac{\sum_{\mathrm{object}} (I - I_{\mathrm{ref}})^2}{N_{\mathrm{object}}} - \left(\frac{\sum_{\mathrm{object}} (I - I_{\mathrm{ref}})}{N_{\mathrm{object}}} \right)^2}, \tag{14}$$

where I_{ref} is the reference image to which the image I is compared, N_{object} is the number of pixels in the object. This root mean square error was normalized with respect to the standard deviation of the noise. In this way, $\mathrm{NRMSE}_{\mathrm{object}}(I)$ is equal to 1 when the two images are identical apart from the noise. A measure of the ability of the algorithm to reduce the artefact was defined as the reduction rate R_{NRMSE}

$$R_{\mathrm{NRMSE}} = 100 \times \frac{\mathrm{NRMSE}_{\mathrm{object}}(I_{\mathrm{art}}) - \mathrm{NRMSE}_{\mathrm{object}}(I_{\mathrm{corr}})}{\mathrm{NRMSE}_{\mathrm{object}}(I_{\mathrm{art}}) - 1}, \tag{15}$$

where I_{art} and I_{corr} are the images before and after motion correction, respectively. So, $R_{\mathrm{NRMSE}} = 100\%$ if the artefacts are reduced to a level below the acquisition noise. This ratio was evaluated for three noise levels $\mathrm{SNR}_I = \{1000, 100, 50\}$ to assess the sensitivity of the algorithm to the noise. For each noise level, 100 datasets were simulated with different sets of motion parameters ($\sigma_\alpha = 0.5°$ and $\sigma_T = 0.25$ pixel as previously mentioned). Results are presented in the next paragraphs, following the natural order of the algorithm, firstly the translation correction, secondly the rotation correction and finally the global artefact reduction rate.

3.3.1. Performance of the translation correction

The performance of the translation correction was assessed by means of simulations involving intra-scan translations and rotations. Therefore, the translation correction step provides at best an image presenting rotation distortions only. The R_{NRMSE} was calculated using the reference image I_{ref}, reconstructed with the 2D-FFT applied on the signal sampled on the G_α grid. For each SNR_I value, the correction of the translation effect was considered in three cases. First, the translation correction was performed knowing the true sampling grid G_α. This case illustrates the ideal one. Then, to evaluate the efficiency of the SNR_T threshold, the algorithm was applied using the estimated grids $\hat{G}_\alpha$ and $\tilde{G}_\alpha$.

The performances of the translation correction are summarized in the first three columns of Table 1. The reduction rate of the translation artefacts ranges between 82 and 97% depending on SNR_I. These results show that the translation correction step is able to reduce the artefacts almost completely even at low signal-to-noise ratio. We note that the estimation error on the rotation angles affects the translation correction, but the performance is almost restored when the noise threshold SNR_T is applied for the rotation estimation.

3.3.2. Performance of the rotation correction

To reconstruct the images from signals sampled on the irregular grids G_α, $\hat{G}_\alpha$ and $\tilde{G}_\alpha$, the Bayesian estimator was used. The middle three columns of Table 1

Table 1
Reduction rate R_{NRMSE} (%) of the motion artefacts

SNR_I	Sampling grids								
	Translation			Rotation			Global		
	G_α	$\hat{G}_\alpha$	$\tilde{G}_\alpha$	G_α	$\hat{G}_\alpha$	$\tilde{G}_\alpha$	G_α	$\hat{G}_\alpha$	$\tilde{G}_\alpha$
1000	97.1	97.1	**97.1**	97.2	96.8	**96.8**	96.4	96.4	**96.4**
100	95.9	95.0	**95.0**	69.3	51.7	**52.0**	93.5	91.3	**91.4**
50	87.8	81.9	**84.8**	—	—		82.9.	58.7	**76.0**

Reduction rate R_{NRMSE} (%) of the motion artefacts for $\mathrm{SNR}_I = \{1000, 100, 50\}$ and for the different steps of our algorithm. The reduction rate was calculated for the different acquisition grids: G_α the simulated acquisition grid and the estimated grid $\hat{G}_\alpha$ and $\tilde{G}_\alpha$, using, respectively, no noise-threshold ($\mathrm{SNR}_T = 0$) and a noise-threshold ($\mathrm{SNR}_T = 2.7$); $\sigma_\alpha = 0.5°$ and $\sigma_T = 0.25$ pixel.

summarize the performance of the rotation correction. The performance of the Bayesian algorithm was assessed by computing R_{NRMSE} for the three grids. The reference image I_{ref} thereby used was the motion-free image reconstructed by 2D-FFT. For high values of the SNR_I ($\mathrm{SNR}_I = 1000$), the angles estimated by the rotation estimator and the Bayesian image reconstruction permit almost complete recovery of the rotation-free image ($R_{\mathrm{NRMSE}} = 96.8\%$). For lower SNR_I, the performance appears to be reduced ($\mathrm{SNR}_I = 100$) or difficult to interpret ($\mathrm{SNR}_I = 50$). This is due to the fact that the background noise in the image has an intensity similar to the rotation artefacts. The artefacts generated by rotation are slightly higher than the noise for $\mathrm{SNR}_I = 100$ and smaller or equal at $\mathrm{SNR}_I = 50$.

To illustrate the efficiency of the Bayesian image reconstruction, we present in Fig. 4 brain images (128×128) distorted by simulated rotations (in this case, the standard deviation of the rotation angles is 2°) and reconstructed with three different algorithms: the inverse fast Fourier transform (IFFT), the conventional gridding algorithm and IFFT; and the Bayesian estimator. For the gridding (conventional and reverse) and Bayesian algorithms, a Kaiser–Bessel window with a width $L = 5$ and an overgridding factor $f_{\mathrm{og}} = 2$ was used. For optimal accuracy, the value of the shape parameter B of the window was chosen so that $B = (f_{\mathrm{og}} - 0.5)\pi L$ [19,22–24]. For the conventional gridding algorithm, the sampling density compensation has been estimated using Voronoi's cell computation [12,35,37] based on geometrical considerations.

The reduction rate R_{NRMSE} calculated from these images show that the artifacts are reduced by only 44% with the conventional gridding algorithm based on Voronoi's sampling density compensation and by 95% with the Bayesian estimator, with respect to the reconstructed IFFT image.

Another illustration of the efficiency of our Bayesian estimator to reconstruct images from rotation-corrupted k-spaces is shown in Fig. 1. A noiseless Shepp–Logan phantom in the k-space with intra-scan rotations was simulated by rotating each trajectory of k-space with

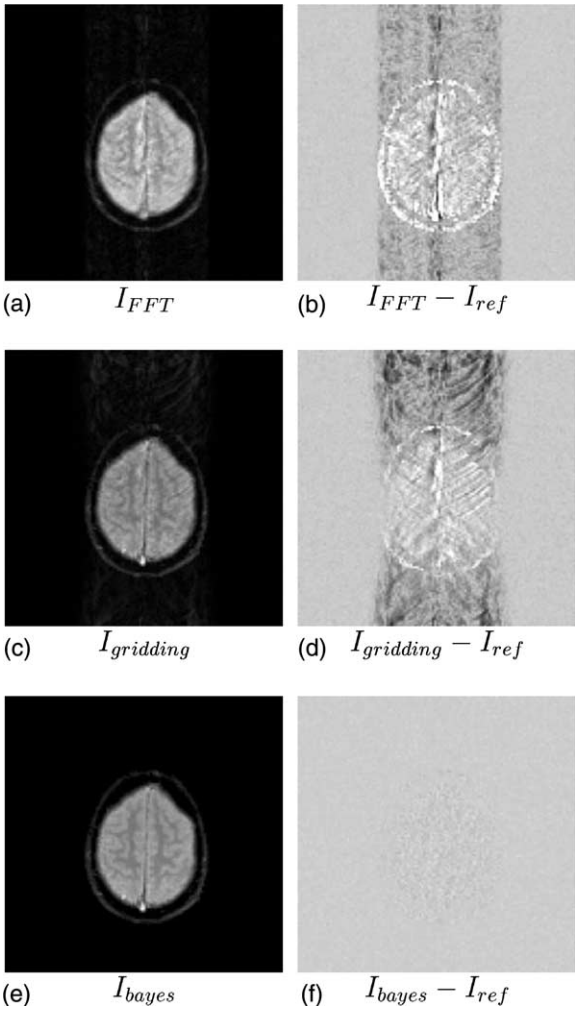

Fig. 4. Illustration of the efficiency of the Bayesian estimator for the image reconstruction. Random rotation effects were introduced by simulation in a brain acquisition. The standard deviation of the rotation angles is 2°. This distorted acquisition was reconstructed with three different algorithms: the IFFT (a), the gridding algorithm and IFFT (c) and the Bayesian estimator (e). Images (b,d,f) show the difference between each reconstructed image and the rotation-free reference image. The ratios R_{NRMSE} associated with the images reconstructed with the gridding algorithm and the Bayesian estimator are, respectively, 44 and 95%.

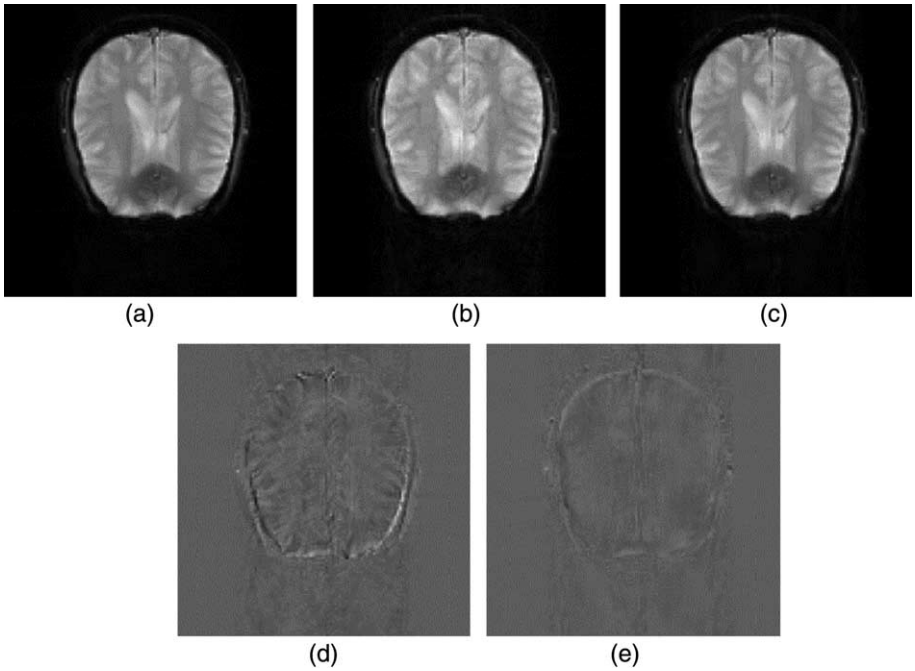

Fig. 5. Intra-scan motion correction of a brain scan acquired with a GRE sequence (TE/TR = 40/2000 ms). (a) Reference image. (b) Motion distorted image. The subject has been requested to rotate the head around the caudo-cranial axis between successive profile measurements in k-space. (c) Motion-corrected image. (d) Difference image (b–a). (e) Difference image (c–a), the reduction of motion artefacts is clearly visible. The reduction rate R_{NRMSE} equals 50%.

random angles having a Gaussian distribution ($\mu = 0$, $\sigma = 1.0°$) [12,16], see Fig. 1c. The k-space estimated by our Bayesian estimator is shown in Fig. 1d and exhibits no difference with the k-space sampled onto the Cartesian grid.

3.3.3. Global performance of the algorithm

The overall performance of the method, i.e., after correction of the translation and rotation effects, is also presented in Table 1. The reduction rates R_{NRMSE} are computed using the motion-free image I_{ref} as reference. The algorithm is able to reduce the intensity of motion artefacts by 96% at high SNR_I and by 76% at low SNR_I. The use of the estimated acquisition grid $\tilde{G}_\alpha$ (using $\mathrm{SNR}_{\mathrm{T}}$) instead of $\hat{G}_\alpha$ improves significantly the performance of the method at $\mathrm{SNR}_I = 50$. The global performance is better than the rotation correction performance because with the particular parameters chosen, the translation artefacts are stronger than the rotation artefacts.

The efficiency of the proposed algorithm to restore images from motion-corrupted data is qualitatively illustrated in Fig. 5. Two data sets have been acquired with a gradient-recalled echo (GRE) sequence (TE/TR = 40/2000 ms). During the first acquisition, the subject has been asked not to move. This data set serves as the reference k-space acquisition. During the second acquisition, the subject has been requested to rotate the head around the caudo-cranial axis between successive profile measurements in k-space. Fig. 5a shows the reference image. In Fig. 5b, motion artefacts are visible at the bottom of the image. They are more visible in the difference image (b–a) in Fig. 5d. Fig. 5c shows the image after motion correction and Fig. 5e, the difference image (c–a). Reduction of motion artefacts is clearly visible. Quantitatively, the reduction rate R_{NRMSE} equals 50%.

4. Discussion

The goal of this paper was to develop a novel algorithm for restoring images from data corrupted by subject motion during the acquisition. We have presented a powerful and automatic method for accurately estimating the intra-scan motion parameters and reconstructing the image from the estimated sample positions. The method relies on the information in k-space only. In order to reconstruct an image from data distorted by rotations, we used a Bayesian estimator which has proven particularly efficient in handling pseudo-randomly sampled and under-sampled k-spaces. The accuracy of motion estimates assessed by Monte Carlo studies is excellent, better than 0.1° for rotation, and 0.1 and 0.05 pixel, respectively, for translation along the read and phase directions for signal-to-noise ratios higher than 6 of the signals on each trajectory. The algorithm reduces the distortion due to rotation down to the noise level.

Estimation of intra-scan motion parameters requires a reference image. Since motion can distort all images within a series, using one of the images of the series as a reference allows correction of *relative* intra-scan motion only. It is therefore obvious that the quality of the correction will critically depend on the quality of the reference image. Conversely, if the reference image is motion-free, *absolute* motion correction is possible. Our algorithm corrects, in a first step, the effects due to intra-scan translation that occurred during acquisition of the reference image. This significantly improves the subsequent estimation of the rotation parameters [35].

Conceptually, our 2D method may be extended to 3D EPI-like acquisitions. If intra-scan motion during the signal read-out is neglected (a reasonable assumption, given the short signal readout times), rotation will affect orientation of the acquisition planes in k-space, while translation will introduce a linear phase shift along the corresponding reciprocal direction. Thus, motion results in irregular sampling of 3D k-space and the tilted linear trajectories in the 2D case now become tilted planes. Six motion parameters per plane (three for translation and three for rotation) need then to be estimated. The extension to 3D raises the issue of computational efficiency to estimate these six parameters, in particular the rotation angles. The 3D gridding or chirp-z algorithm [38] could therefore be used in the rotation estimation step to rotate the reference acquisition. The reconstruction of the 3D images from irregularly sampled k-space could then be handled by our 3D version of the Bayesian estimator [27,39].

Potential applications of the method may lie in 3D EPI-like fMRI. Also, the quality of averaged imaging volumes should benefit from applying intra-scan motion correction.

Acknowledgments

The authors thank Dr. Simon Doran for critical review of the manuscript. The study has been supported by the European Union (Programmes TMR, Networks, ERB-FMRX-CT97-0160, and BIOMED II PL950870) and by the Région Rhône-Alpes (France).

References

[1] M. Hedley, H. Yan, D. Rosenfeld, An improved algorithm for 2-D translational motion artifact correction, IEEE Trans. Med. Imaging 10 (1991) 548–553.

[2] M. Hedley, H. Yan, D. Rosenfeld, Motion artifact correction in MRI using generalized projections, IEEE Trans. Med. Imaging 10 (1991) 40–46.

[3] R.A. Zoroofi, Y. Sato, S. Tamura, H. Naito, An improved method for MRI artifact correction due to translational motion in the imaging plane, IEEE Trans. Med. Imaging 14 (1995) 471–479.

[4] L. Tang, M. Ohya, Y. Sato, H. Naito, K. Harada, S. Tamura, Cancellation of motion artifact in MRI due to 2D rigid translation motion, Comput. Biol. Med. 27 (1997) 211–222.

[5] H.W. Korin, J.P. Felmee, S.J. Riederer, R.L. Ehman, Spatial-frequency-tuner markers and adaptative correction for rotational motion, Magn. Reson. Med. 33 (1995) 663–669.

[6] Z.W. Fu, Y. Wang, R.C. Grimm, P.J. Rossman, J.P. Felmlee, S.J. Riederer, R.L. Ehman, Orbital navigator echoes for motion measurements in magnetic resonance imaging, Magn. Reson. Med. 34 (1995) 746–753.

[7] R.C. Grimm, S.J. Riederer, R.L. Ehman, Real-time rotation correction using orbital navigator echoes, in: Proceedings of the 5th Scientific Meeting of the ISMRM, Vancouver, Canada, 1997, p. 1899.

[8] E.B. Welch, A. Manduca, R.C. Grimm, H.A. Ward, C.R. Jack, Spherical navigator echoes for full 3D rigid body motion measurement in MRI, Magn. Reson. Med. 47 (2002) 32–41.

[9] R.A. Zoroofi, Y. Sato, S. Tamura, H. Naito, MRI artifact cancellation due to rigid motion in the imaging plane, IEEE Trans. Med. Imaging 15 (1996) 768–784.

[10] D. Atkinson, D.L.G. Hill, P.N.R. Stoyle, P.E. Summers, S.F. Keevil, Automatic correction of motion artifacts in Magnetic Resonance images using an entropy focus criterion, IEEE Trans. Med. Imaging 16 (1997) 903–910.

[11] C. Weerasinghe, H. Yan, An improved algorithm for rotational motion artifact suppression in MRI, IEEE Trans. Med. Imaging 17 (1998) 310–317.

[12] M. Bourgeois, F.T.A.W. Wajer, D. van Ormondt, D. Graveron-Demilly, In Book: Modern Sampling Theory: Mathematics and Applications, Birkhäuser, Basel, 2001, Ch. 16, J.J. Benedetto, P.J.S.G. Ferreira (Eds.), Reconstruction of MRI Images from Non-Uniform Sampling: Application to Intrascan Motion Correction in Functional MRI, pp. 343–362.

[13] C. Weerasinghe, L. Jan, H. Yan, In Book: Signal Processing for Magnetic Resonance Imaging and Spectroscopy, Marcel Dekker, New York, 2002, Ch. 5, H. Yan (Ed.), Rotational Motion Artifact Correction based on Fuzzy Projection onto Convex Sets, pp. 125–166.

[14] A.M. Ulug, P.B. Baker, P.C.M. van Zijl, Correction of motional artifacts in diffusion-weighted images using a reference phase map, Magn. Reson. Med. 34 (1995) 476–480.

[15] M. Bourgeois, Y. Crémillieux, C. Delon-Martin, M. Roth, A. Briguet, D. Graveron-Demilly, Analysis and correction of in-plane intrascan rotation artefacts, in: Proceedings of the 5th Scientific Meeting of the ISMRM, Vancouver, BC, Canada, 1997, p. 1908.

[16] M. Bourgeois, F.T.A.W. Wajer, G.H.L.A. Stijnman, Y. Crémillieux, D. van Ormondt, A. Briguet, D. Graveron-Demilly, Reduction of random in plane intrascan rotation artefacts, in: Proceedings of the 6th Scientific Meeting of the ISMRM, Sydney, Australia, 1998, p. 1963.

[17] D. Atkinson, D.L.G. Hill, Automatic motion correction using prior knowledge, in: Proceedings of the 9th Scientific Meeting of the ISMRM and 18th Scientific Meeting of the ESMRMB, Glasgow, 2001, p. 747.

[18] F.T.A.W. Wajer, R. de Beer, M. Fuderer, A.F. Mehlkopf, D. van Ormondt, Bayesian Image Reconstruction from arbritrarily sampled k-space without density correction, in: Proceedings of the 6th Scientific Meeting of the ISMRM, Sydney, Australia, 1998, p. 667.

[19] F.T.A.W. Wajer, G.H.L.A. Stijnman, M. Bourgeois, D. Graveron-Demilly, D. van Ormondt, In Book: Nonuniform Sampling, Theory and Practice, Kluwer/Plenum, Dordrecht/New York, 2001, Ch. 10, F.A. Marvasti (Ed.), Magnetic Resonance Image Reconstruction from Nonuniformly Sampled k-space Data, pp. 439–478.

[20] M. Hedley, H. Yan, D. Rosenfeld, A modified Gerchberg–Saxton algorithm for one-dimensional motion artifact correction in MRI, IEEE Trans. Signal Process. 39 (1991) 1428–1433.
[21] H. Schomberg, J. Timmer, A gridding method for image reconstruction by Fourier transformation, IEEE Trans. Med. Imaging 14 (1995) 596–607.
[22] F.T.A.W. Wajer, D. van Ormondt, M. Bourgeois, D. Graveron-Demilly, Nonuniform sampling in Magnetic Resonance Imaging, ICASSP, IEEE International Conference on Acoustics, Speech, and Signal Processing. Istanbul, 5-9 june 2000, in: IEEE, Piscataway, NJ, USA, 2000, pp. 3846–3849.
[23] F.T.A.W. Wajer, R. Lethmate, J.A.C. van Osch, D. Graveron-Demilly, M. Fuderer, D. van Ormondt, Interpolation from arbitrary to Cartesian sample positions: gridding, in: J.-P. Veen (Ed.), Proceedings ProRISC, Workshop on Circuits, Systems, and Signal Processing, STW Technology Foundation, 2000, pp. 571–577. Available from <http://www.stw.nl/programmas/prorisc/index.html>.
[24] F.T.A.W. Wajer, R. Lethmate, J.A.C. van Osch, D. Graveron-Demilly, D. van Ormondt, Simple formula for the accuracy of gridding, in: 9th Scientific Meeting of the ISMRM and 18th Scientific Meeting of the ESMRMB, Glasgow, Scotland, UK, 2001, p. 776.
[25] D. Graveron-Demilly, G.J. Marseille, Y. Crémillieux, S. Cavassila, D. van Ormondt, SRS-FT: a Fourier imaging method based on sparse radial scanning and Bayesian estimation, J. Magn. Reson. B 112 (1996) 119–123.
[26] F.T.A.W. Wajer, A. Coron, R. Lethmate, J.A.C. van Osch, L.T. Martinez, D. Graveron-Demilly, D. van Ormondt, Accelerated Bayesian MR Image Reconstruction, in: Proceedings of the 10th Scientific Meeting of the ISMRM, Honolulu, Hawaii USA, 2002, p. 2422.
[27] F.T.A.W. Wajer, A. Coron, R. Lethmate, J.A.C. van Osch, L.T. Martinez, D. Graveron-Demilly, D. van Ormondt, Accelerated Bayesian MR Image Reconstruction, in: Proceedings ProRISC, Workshop on Circuits, Systems, and Signal Processing, STW Technology Foundation, 2001, pp. 721–727. Available from <http://www.stw.nl/programmas/prorisc/index.html>.
[28] F.T.A.W. Wajer, Non-Cartesian MRI scan time reduction through sparse sampling, Ph.D. Thesis, Delft University of Technology—TUD, Delft, The Netherlands. Available from <http://www.library.tudelft.nl/dissertations/> (2001).
[29] M. Fuderer, Ringing artefact reduction by an efficient likelihood improvement method, in: Proc. SPIE, vol. 1137, 1989, pp. 84–90.
[30] G.J. Marseille, M. Fuderer, R. de Beer, A.F. Melkopf, D. van Ormondt, Reduction of MRI scan time through nonuniform sampling and edge-distribution modeling, J. Magn. Reson. B 103 (1994) 292–295.
[31] S. Geman, D.E. McClure, Statistical methods for tomographic image reconstruction, Bull. Int. Statist. Inst. 4 (1987) 5–21.
[32] A.H. Lettington, Q.H. Hong, Image restoration using a Lorentzian probability model, J. Modern Opt. 42 (1995) 1367–1376.
[33] G. Sebastiani, F. Godtliebsen, On the use of Gibbs priors for Bayesian image restoration, Signal Process. 56 (1997) 111–118.
[34] L.A. Shepp, B.F. Logan, The Fourier reconstruction of a head section, IEEE Trans. Nucl. Sci. 21 (1974) 21–43.
[35] M. Bourgeois, Correction des mouvements intra-image en imagerie d'activation cérébrale par résonance magnétique, Ph.D. Thesis, Université Claude Bernard, Lyon, 1999.
[36] H. Gudbjartsson, S. Patz, The Rician distribution of noisy MRI data, Magn. Reson. Med. 34 (1995) 910–914.
[37] A. Okabe, B. Boots, K. Sugihara, Spatial Tessellations: Concepts and Applications of Voronoi Diagrams, Wiley, New York, 1992.
[38] R. Tong, R.W. Cox, Rotation of NMR images using the 2D chirp-z transform, Magn. Reson. Med. 41 (1999) 253–256.
[39] L.T. Martinez, F.T.A.W. Wajer, R. Lethmate, R.A.J. de Jong, G.H.L.A. Stijnman, Y. Crémillieux, D. van Ormondt, D. Graveron-Demilly, Sparse 3D Radial Scanning and Bayes Reconstruction, in: Proceedings of the 8th Scientific Meeting of the ISMRM, Denver, USA, 2000, p. 1723.